Dynamics of a liquid film sheared by a co-flowing turbulent gas

Rajagopal Vellingiri[a], Dmitri Tseluiko[b], Nikos Savva[a,c], Serafim Kalliadasis[a,*]

[a] *Department of Chemical Engineering, Imperial College London, London SW7 2AZ, United Kingdom*
[b] *School of Mathematics, Loughborough University, Loughborough LE11 3TU, United Kingdom*
[c] *School of Mathematics, Cardiff University, Cardiff CF24 4AG, United Kingdom*

Abstract

Consider the dynamics of a thin laminar liquid film flowing over an inclined wall in the presence of a co-flowing turbulent gas. The solution to the full two-phase flow problem poses substantial technical difficulties. However, by making appropriate assumptions, the solution process can be simplified and can provide valuable insights. The assumptions allow us to solve the gas and liquid problems independently. Solving for the gas flow reduces to finding perturbations to pressure and tangential stresses at the interface, influencing the liquid problem through the boundary conditions. We analyze the effect of gas flow on the liquid problem by developing an integral-boundary-layer model, which is valid up to moderate liquid Reynolds numbers. We seek solitary-wave solutions of this model under the influence of gas flow via a pseudo-arclength continuation method. Our computations demonstrate that as a general trend, the wave speed increases with increasing the gas shear and the liquid flow rate. Further insight into the problem is provided via time-dependent computations of the integral-boundary-layer model.

Keywords: Liquid film, Gas shear, Solitary waves, Co-current flow, Numerical continuation

1. Introduction

Gas-liquid flows are ubiquitous in nature, such as the shearing of the sea- and lake-water by the air flowing over it. They are also central in a wide spectrum of engineering applications. For instance, in chemical engineering, gas-liquid flows are commonly observed in the transport of hydrocarbons through long distance pipelines, absorption and distillation processes, and in a wide spectrum of processes and devices. The associated rate of heat and mass transport is significantly influenced by the hydrodynamic and physico-chemical phenomena occurring on the interfaces, hence the study

*Corresponding author
Email address: s.kalliadasis@imperial.ac.uk (Serafim Kalliadasis)

of interfacial effects becomes crucial for practical applications. An accurate description of the gas-liquid interface, that in turn depends on the liquid and gas flow structure, is also essential from the fundamental point of view to e.g. understand the various transitions occurring in the wave formation process associated with the destabilization of the interface.

The flow of a thin liquid film on an inclined plate has been the subject of many studies for a long time since the pioneering experiments of Kapitza (1965). This seemingly simple physical system can exhibit a rich dynamical behavior starting from a laminar initial film, a sequence of wave families on the surface of the film, such as periodic traveling waves and solitary waves, and eventually spatiotemporal chaos through a series of bifurcations between the different wave families. For small to moderate values of the Reynolds number, the free surface is essentially two-dimensional, comprising of solitary waves which are formed as a result of the primary wave field undergoing a secondary instability. These solitary waves have been observed in many experimental (Liu and Gollub, 1994; Vlachogiannis and Bontozoglou, 2001) and theoretical studies (Chang et al., 1995; Malamataris and Balakotaiah, 2008). Extensive reviews of falling liquid film studies can be found in the monographs by Alekseenko et al. (1994), Chang and Demekhin (2002) and Kalliadasis et al. (2011).

One of the earliest works on co-current gas-liquid film flows was that of Hanratty and Engen (1957), where the interaction between a co-flowing turbulent air stream and a thin water film was investigated experimentally. These authors reported the transition from a smooth surface to two-dimensional waves, and further to "pebbled" surfaces. Craik (1966) studied experimentally thin water films of thickness 0.13-1.6 mm in a horizontal rectangular channel, and reported the presence of fast and slow waves, that traveled faster and slower than the interface, respectively. Cohen and Hanratty (1965), through a combination of theory and experiments, analyzed a co-flowing glycerine-water solution with air in a horizontal channel. They had made use of the model of Miles (1957) and Benjamin (1959) to calculate the shear stress and pressure variations from their experimental data, and reported that the interfacial waves tend to decay, when the rate of energy transfer from the gas to the liquid is smaller than the viscous dissipation taking place within the liquid. Woodmansee and Hanratty (1969) attempted to connect the droplet entrainment from a liquid film in a horizontal co-current setting with the appearance of roll waves, which is typically marked by a sudden increase in the thickness of the liquid layer. Moreover, according to these authors, it is the imbalance in the pressure variations in the gas phase flowing over the wavelets, and the stabilizing effect of gravity and surface tension that leads to the entrainment of droplets from the liquid film.

Lioumbas et al. (2005) investigated the stratified co-current gas-liquid film flow in an inclined

channel by experiments. The experiments were conducted at high liquid Reynolds numbers and for small inclination angles. They observed that for a given gas flow rate, small amplitude waves that exist at relatively low liquid Reynolds numbers transform to solitary waves as the Reynolds number is increased beyond a critical value. However, for large gas and liquid velocities, roll waves having a large amplitude and moving at high speed, start to appear. In their subsequent studies, Lioumbas et al. (2006, 2009) analyzed the influence of surfactants on the wave characteristics of both the upflow and downflow configurations in inclined channels. In a recent experimental study, Alekseenko et al. (2009) investigated both the entrainment and no-entrainment regimes of gas-liquid annular flows, and attempted to link the occurrence of entrainment phenomena, with the disappearance of ripples that were previously formed on the backward slope of disturbance waves.

Theoretical studies of co-current gas-liquid film flows are limited. Jurman and McCready (1989) investigated theoretically and experimentally waves on thin liquid films sheared by a turbulent gas in a horizontal setting. In their analysis on glycerine-water solution system, they reported the existence of solitary waves that travel faster than the periodic waves, when the gas Reynolds number is sufficiently large till a critical liquid Reynolds number is reached. They supplemented their experimental analysis by deriving a weakly nonlinear model using boundary-layer-type approximations, and examined the influence of dynamic and kinematic processes on the wave behavior. In their predominantly experimental study on a co-current gas sheared liquid flow problem in a horizontal setting, Peng et al. (1991) looked at the wave field both for low liquid Reynolds numbers, where solitary waves exist, and high Reynolds numbers, where solitary waves are absent. They conjectured that solitary waves originate from waves that have sufficiently large amplitude to substrate depth ratios, through a secondary transition. More recently, Frank (2006) demonstrated numerically by using the method of particles, the existence of solitary waves in a shear driven thin film flow in a horizontal channel in the presence of laminar gas flow.

The present study builds on the methodology developed by Tseluiko and Kalliadasis (2011)(referred to as TK in the following) to analyze flooding in a countercurrent gas-liquid film flow. We concentrate here on the influence of gas shear on the structure and speed of solitary waves with a gas co-flowing over a thin liquid film in a vertical channel. As part of the analysis presented here parallels the work of TK, when necessary the reader will be referred to this study for further details. For the co-current problem considered here, we solve the gas and liquid problems separately by making appropriate assumptions as in the study of TK. The gas problem in particular, is analyzed with an improved version of the quasi-laminarity approach of Miles (1957) and Benjamin (1959), which is also used by Demekhin

(1981) and Trifonov (2010) but on a Cartesian coordinate system. Like in TK, we work on curvilinear boundary layer coordinates, and find perturbations to pressure and tangential stresses at the interface due to the turbulent gas flow, which are used as boundary conditions in the solution to the liquid flow problem. Instead of solving the full Navier-Stokes equation for the liquid problem, as done by Trifonov (2010), we develop an integral-boundary-layer (IBL) model, that has the advantage of being amenable to mathematical and numerical analysis for moderate Reynolds numbers. In particular, the integral-boundary-layer model of Ruyer-Quil and Manneville (1998, 2000) for free-falling liquid films, obtained by combining the long-wave approximation with a polynomial expansion for the velocity field, with the integral-boundary-layer approximation and the method of weighted residuals, is known to describe nonlinear waves sufficiently far from criticality. This approach was further extended to falling film problems with additional complexities like thermocapillary Marangoni effects (Kalliadasis et al. (2003), Scheid et al. (2005a), Scheid et al. (2005b)), solutocapillary Marangoni effects induced by chemical reactions (Trevelyan and Kalliadasis (2004); Trevelyan et al. (2012)) and insoluble surfactants (Pereira and Kalliadasis (2008)).

Our study is structured as follows. In Section 2 we describe the problem set up and in Section 3 we solve the gas problem. An IBL model is developed in Section 4, which is also used to perform a linear stability analysis of the flat film solution in contact with the gas flow. Using the IBL model we discuss solitary-wave solutions in Section 5 through a continuation approach, and time-dependent computations in 6. Finally, we summarize our findings in Section 7.

2. Problem setting

We consider a thin liquid film flowing down a smooth solid plate under the action of gravity as shown in Fig. 1. Let θ denote the inclination angle of the solid plate with respect to the horizontal, and ρ_ℓ and μ_ℓ the density and viscosity of the liquid, respectively. A gas of density ρ_g and viscosity μ_g, confined between the gas-liquid interface below and a planar solid wall at the top, flows in the downward direction (say, as a result of being pumped from the top). We take the width of the channel occupied by the gas to be much larger than the liquid film thickness, assuming also that the gas flows much faster than the liquid, hence the gas is taken to be turbulent whereas the liquid is taken to be laminar. Let the velocity and pressure in the liquid side be $\tilde{\mathbf{u}}$ and $\tilde{p}$, respectively, and the mean velocity and pressure in the gas side be $\widetilde{\mathbf{U}}$ and $\tilde{P}$, respectively. We assume that both the liquid and the mean gas flow are two-dimensional so that there are no variations in the transverse direction. Let

$(\tilde{x},\, \tilde{y})$ be a Cartesian coordinate system with the $\tilde{x}$-axis pointing downwards along the wall. Let the gas-liquid interface be located at $\tilde{y} = \tilde{h}(\tilde{x}, \tilde{t})$, and let the thickness of the liquid film when the interface is undisturbed be $\tilde{h}_0$. The distance between the undisturbed interface and the upper solid wall is taken to be $2\tilde{L}$.

Solving this coupled gas-liquid system is difficult, if not prohibitive. However, the problem becomes relatively simpler and analytical progress can be made by making use of the fact that the viscosity of the gas is much smaller than that of the liquid ($\mu_g \ll \mu_\ell$), followed by a series of additional reasonable assumptions, namely that the velocity in the liquid layer is much smaller than the mean velocity in the gas layer and that the turbulent fluctuations in the gas flowing over the liquid film decay in the same way as those in the gas flowing over a rigid wall. Under these assumptions, the gas and liquid problems can be solved independently, as in TK. In fact, the analysis in Sections 3-4 follows closely to that in TK for the counter-current case, but for clarity and ease of presentation we reiterate the main steps here.

[Figure 1 about here.]

3. Gas problem

We model the turbulent nature of flow by assuming the gas flow to be quasi-steady, and applying appropriate averaging. We then obtain the following incompressible Reynolds-averaged Navier-Stokes (RANS) equation together with the equation for mass conservation (Schlichting (2000)):

$$\rho_g \widetilde{\mathbf{U}} \cdot \boldsymbol{\nabla} \widetilde{\mathbf{U}} = -\boldsymbol{\nabla} \widetilde{P} + \mu_g \boldsymbol{\nabla}^2 \widetilde{\mathbf{U}} + \boldsymbol{\nabla} \cdot \widetilde{\boldsymbol{\sigma}}, \qquad \boldsymbol{\nabla} \cdot \widetilde{\mathbf{U}} = 0, \tag{1}$$

where $\widetilde{\mathbf{U}} = (\widetilde{U}, \widetilde{V})$ and $\widetilde{P}$ are the mean velocity and pressure fields in the gas phase, respectively, $\boldsymbol{\nabla} = (\partial/\partial\tilde{x}, \partial/\partial\tilde{y})$, $\widetilde{\boldsymbol{\sigma}}$ is the Reynolds stress tensor coming from the contribution of turbulent fluctuations, whereas $\mu_g \boldsymbol{\nabla}^2 \widetilde{\mathbf{U}}$ originates from the viscous stress tensor.

The boundary conditions supplementing Eq. (1) are the no-slip and no-penetration conditions at the upper planar wall and the lower wavy wall that corresponds to the liquid-gas interface:

$$\widetilde{\mathbf{U}} = \mathbf{0} \quad \text{at} \quad \tilde{y} = \tilde{h}_0 + 2\tilde{L} \quad \text{and} \quad \tilde{y} = \tilde{h}_0 + \tilde{s}(\tilde{x}), \tag{2}$$

where $\tilde{s}(\tilde{x}) = \tilde{\epsilon} e^{\mathrm{i}\tilde{\alpha}\tilde{x}}$, and $\tilde{\epsilon}$ and $\tilde{\alpha}$ correspond to the amplitude and wavenumber of the undulating wall (the liquid-gas interface), respectively. We also note here that the real part of $\tilde{s}(\tilde{x})$ represents

the actual physical wall. To non-dimensionalize the equations, we choose, respectively, the following velocity, length and pressure scales:

$$U_f^* = \sqrt{\frac{T_w}{\rho_g}}, \quad L_c = \frac{\mu_g}{\rho_g U_f^*}, \quad P_c = \rho_g U_f^{*2}, \tag{3}$$

where T_w is the shear stress at the lower wall when the wall is flat, and U_f^* is the friction velocity. Furthermore, we define the normal coordinate y to be $y = (\tilde{y} - \tilde{h}_0)/L_c$, such that $y = 0$ corresponds to the undisturbed wall.

The resulting equations and boundary conditions in non-dimensional form are given by

$$UU_x + VU_y = -P_x + U_{xx} + U_{yy} + \tau_{11x} + \tau_{12y}, \tag{4a}$$

$$UV_x + VV_y = -P_y + V_{xx} + V_{yy} + \tau_{21x} + \tau_{22y}, \tag{4b}$$

$$U_x + V_y = 0, \tag{4c}$$

$$U = V = 0 \quad \text{at} \quad y = s(x) \quad \text{and} \quad y = 2L. \tag{5}$$

The gas-liquid interface is prescribed in dimensionless form by $y = s(x) \equiv \epsilon e^{\mathrm{i}\alpha x}$, where $\epsilon (= \tilde{\epsilon}/L_c) \ll 1$, and $\alpha = \tilde{\alpha}/L_c$. To proceed, we look for a unidirectional velocity profile when the lower wall is assumed to be undisturbed. In order to model the turbulent stress there exist a number of approaches, but we choose the mixing length route, as one of our main objectives is to use a simple model that gives good agreement with experiments (e.g. flow over undulated walls) and allows us to make analytical progress. We set $\tau_{0\,11} = \tau_{0\,22} = 0$ and $\tau_{0\,12} = \tau_{0\,21} = \ell^2 |U_{0y}| U_{0y}$ (here subscripts 0 indicate the base solution for the flat interface). To model the mixing length ℓ, we consider the equation of van Driest, as the variation of mixing length over the entire cross section can be very well described by this model for wall bounded flows. The van Driest equation is given by $\ell = \kappa y \left[1 - e^{-y/A}\right]$, where $\kappa = 0.41$ is the von Kármán constant and the parameter A is a measure of the thickness of the viscous region close to the wall. The parameter A was considered to be a function of the pressure gradient by Thorsness et al. (1978), however taking A to be a constant is sufficient to obtain good agreement with experiments for flow over wavy walls (see TK). Therefore, we set the value of A to 25, that was determined from the fit of experimental data for the flow over a flat wall (see Van Driest, 1956). It is also important to note that the direction of gas flow (co-current or counter-current) does not play any role in the estimation of A, as the interface appears as a solid wall for the gas problem. Under these conditions, TK have shown that

$$U_0 = \int_0^y \frac{2(L-z)/L}{1 + \sqrt{1 + 4\kappa^2 z^2 [1 - e^{-z/A}]^2 (L-z)/L}} \mathrm{d}z. \tag{6}$$

The velocity profile U_0 for $L = 200$ is shown in Fig. 2.

[Figure 2 about here.]

The gas flow has a layered structure. In the core layer, where $\ell \gg 1$, the turbulent momentum transfer dominates. Sufficiently close to the wall (about 20% of the height of the flow), the velocity profile is logarithmic (known as the universal law of the wall). In the thin wall layer, where $\ell \sim 1$, both molecular and turbulent momentum transport act. There is also a very thin viscous sublayer near the wall, where $\ell \ll 1$, in which turbulent momentum transport can be neglected and the velocity profile is linear (Schlichting (2000)).

This base-state solution obtained by considering the interface to be flat in the Cartesian system will be utilized in our subsequent treatment of the problem in the curvilinear coordinates. We recall that the lower wall of the channel is wavy, whereas the top wall is planar. The solution to the fluid flow problem in such a geometry would become relatively simpler, if we choose to work in a coordinate system that would naturally represent these changing boundaries. This calls for a treatment in the curvilinear coordinate system like the one followed by Benjamin (1959). The curvilinear coordinates ξ_1 and ξ_2 can be written in terms of the cartesian coordinates (x, y) as $\xi_1 = \xi_1(x, y)$ and $\xi_2 = \xi_2(x, y)$. As we move away from the lower wavy wall, we want the coordinate lines ξ_1 and ξ_2 to approach that of the Cartesian system. Benjamin (1959) introduced the following coordinates:

$$\xi_1 = x - \mathrm{i}\epsilon e^{-\alpha\xi_2} e^{\mathrm{i}\alpha x}, \tag{7a}$$

$$\xi_2 = y - \epsilon e^{-\alpha\xi_2} e^{\mathrm{i}\alpha x}. \tag{7b}$$

We could infer from Eq. (7) that $\xi_2 = 0$ represents the lower wavy wall to first order in ϵ. It is to be noted that the real parts of Eqs. (7a)-(7b) represent meaningful coordinates, and complex number notations are used only for convenience in calculations. Details on the derivation of the appropriate curvilinear coordinate system are given in TK.

We proceed by using a stream function formulation for the incompressible RANS equation. Let ψ denote the stream function. Making the use of the fact that the wall amplitude is small and writing the expansions

$$\psi = \psi_0(\xi_2) + \epsilon\psi_1(\xi_2) e^{\mathrm{i}\alpha\xi_1} + \cdots, \tag{8}$$

$$P = P_0 + \epsilon P_1(\xi_2) e^{\mathrm{i}\alpha\xi_1} + \cdots, \tag{9}$$

$$\bar{\tau}_{ij} = \bar{\tau}_{0_{ij}} + \epsilon\bar{\tau}_{1_{ij}}(\xi_2) e^{\mathrm{i}\alpha\xi_1} + \cdots, \tag{10}$$

where ψ_0, P_0 and $\bar{\tau}_{0_{ij}}$ denote the stream function, the pressure and the turbulent Reynolds stresses corresponding to the base solution, we obtain the following equation for ψ_1:

$$\psi_1'''' - 2\alpha^2\psi_1'' + 4\alpha e^{-\alpha\xi_2}\left(\psi_0'''' - \alpha\psi_0'''\right) = -\mathrm{i}\alpha\left[\psi_1\psi_0''' - \psi_0'\left(\psi_1'' - \alpha^2\psi_1 + 2\alpha\psi_0'' e^{-\alpha\xi_2}\right)\right] - \mathcal{R}_1, \quad (11)$$

where,

$$\mathcal{R}_1 = \mathrm{i}\alpha\bar{\tau}_{1_{11}}' - \mathrm{i}\alpha\bar{\tau}_{1_{22}}' + \alpha^2\bar{\tau}_{1_{12}} + \bar{\tau}_{1_{12}}'' + e^{-\alpha\xi_2}\left[2\mathrm{i}\alpha^3\bar{\tau}_{0_{11}} - \mathrm{i}\alpha^2\bar{\tau}_{0_{11}}'\right.$$
$$\left. -2\mathrm{i}\alpha^3\bar{\tau}_{0_{22}} + \mathrm{i}\alpha^2\bar{\tau}_{0_{22}}' - 4\alpha^3\bar{\tau}_{0_{12}} + 2\alpha^2\bar{\tau}_{0_{12}}' + 2\alpha\bar{\tau}_{0_{12}}''\right] \quad (12)$$

(details are given in TK). To solve Eq. (11), we make the assumption that the Reynolds stresses induced by the waviness of the interfacial wall and the normal stresses are zero (Thorsness et al., 1978), i.e., $\bar{\tau}_{1_{11}} = \bar{\tau}_{1_{12}} = \bar{\tau}_{1_{21}} = \bar{\tau}_{1_{22}} = 0$ and $\bar{\tau}_{0_{11}} = \bar{\tau}_{0_{22}} = 0$. This implies,

$$\psi_1'''' - 2\alpha^2\psi_1'' + 4\alpha e^{-\alpha\xi_2}\left(\psi_0'''' - \alpha\psi_0'''\right) = -\mathrm{i}\alpha\left[\psi_1\psi_0''' - \psi_0'\left(\psi_1'' - \alpha^2\psi_1 + 2\alpha\psi_0'' e^{-\alpha\xi_2}\right)\right]$$
$$+ e^{-\alpha\xi_2}\left[2\alpha\bar{\tau}_{0_{12}}'' + 2\alpha^2\bar{\tau}_{0_{12}}' - 4\alpha^3\bar{\tau}_{0_{12}}\right]. \quad (13)$$

The boundary conditions supplementing the above fourth-order differential equation are the no-slip and no-penetration conditions at the wall, given by

$$\psi_1 = 0, \quad \psi_1' = 0, \quad \text{at} \quad \xi_2 = 0. \quad (14)$$

Given that as we move away from the wall the flow approaches the base flow for a sufficiently wide channel, we can impose the conditions

$$\psi_1 = 0, \quad \psi_1' = 0, \quad \text{at} \quad \xi_2 = L. \quad (15)$$

We note that ψ_0 and $\bar{\tau}_{0_{12}}$ come from the base-state solution. Once we know the stream function, we can compute the shear stress at the gas-liquid interface, τ_w, and the pressure at the interface, P_w:

$$\tau_w = 1 + \epsilon\tau_{w1}(\alpha)e^{\mathrm{i}\alpha\xi_1} + \cdots, \quad (16)$$

$$P_w = P_0 + \epsilon P_{w1}(\alpha)e^{\mathrm{i}\alpha\xi_1} + \cdots, \quad (17)$$

where

$$\tau_{w1}(\alpha) = \psi_1''(0) + 2\alpha, \quad (18)$$

$$P_{w1}(\alpha) = \frac{\mathrm{i}}{\alpha}\left[\frac{2\alpha}{L} + 2\alpha^2 - \psi_1'''(0)\right]. \quad (19)$$

Note that unlike the setting of a co-current gas-liquid flow considered here, TK considered the case of a counter-current gas-liquid flow. It can be easily shown that there exists a relation between shear stresses and pressures for the co-current and counter-current flows. Indeed, let $\bar{\tau}_w$ and $\bar{P}_w$ denote the shear stress and the pressure for the counter-current flow over a wavy wall of small amplitude, i.e.

$$\bar{\tau}_w = -1 + \epsilon \bar{\tau}_{w1}(\alpha) e^{\mathrm{i}\alpha\xi_1} + \cdots , \tag{20}$$

$$\bar{P}_w = P_0 + \epsilon \bar{P}_{w1}(\alpha) e^{\mathrm{i}\alpha\xi_1} + \cdots . \tag{21}$$

Keeping in mind that actually real parts represent physical quantities, we must have

$$[P_w(\xi_1)]_R = [\bar{P}_w(-\xi_1)]_R, \tag{22}$$

$$[\tau_w(\xi_1)]_R = -[\bar{\tau}_w(-\xi_1)]_R, \tag{23}$$

which implies that

$$\bar{P}_{w1}(\alpha) = [P_{w1}(\alpha)]^*, \quad \bar{\tau}_{w1}(\alpha) = -[\tau_{w1}(\alpha)]^*, \tag{24}$$

where R in the subscript denotes real part of the complex quantity, and '$*$' denotes complex conjugation. These relations allow us to map the counter-current problem, to the co-current one.

Note also that for the counter-current case, TK compared their theoretical predictions for the shear stress and the pressure imposed by a turbulent gas flowing over a wavy wall with the experimental results of Zilker et al. (1977) and Thorsness et al. (1978) and found good agreement. Moreover, it was found that the analysis in curvilinear boundary layer coordinates gives significantly better agreement with experiments than the analysis in Cartesian coordinates.

Next, we consider the lower wall (corresponding to the interface) to be a periodic function with zero mean and period λ given by

$$s(x) = \sum_{\substack{n=-\infty \\ n\neq 0}}^{\infty} s_n \mathrm{e}^{\mathrm{i}\alpha_n x}, \tag{25}$$

where the wavenumber $\alpha_n = 2\pi n/\lambda$, and s_n are the Fourier coefficients. To obtain expressions for the shear stress and the pressure imposed on such a wall, we make the assumption that these quantities depend linearly on the interface shape. Therefore, the wall shear stress and pressure, are, respectively

$$\tau_w[s] = 1 + \sum_{\substack{n=-\infty \\ n\neq 0}}^{\infty} s_n \tau_{w1}(\alpha_n) \mathrm{e}^{\mathrm{i}\alpha_n x} \tag{26}$$

and

$$P_w[s] = P_0 + \sum_{\substack{n=-\infty \\ n\neq 0}}^{\infty} s_n P_{w1}(\alpha_n) \mathrm{e}^{\mathrm{i}\alpha_n x}. \tag{27}$$

Here, for a negative α_n, we define $\tau_{w1}(\alpha_n) = [\tau_{w1}(-\alpha_n)]^*$ and $P_{w1}(\alpha_n) = [P_{w1}(-\alpha_n)]^*$. For a given $s(x)$, by making use of Eqs. (18), we can compute the shear stress τ_w and the pressure P_w acting on the wall.

4. Liquid problem

Now we introduce the governing equations for the liquid film (for a more detailed discussion of the governing equations for the liquid film sheared by a counter-current turbulent gas we refer the reader to TK). The governing equations are the Navier-Stokes and continuity equations, which we non-dimensionalize using the following velocity, time, pressure and length scales:

$$u_c = \frac{\rho_\ell g \tilde{h}_0^2 \sin\theta}{2\mu_\ell}, \quad t_c = \frac{\tilde{h}_0}{u_c}, \quad p_c = \frac{\mu_\ell u_c}{\tilde{h}_0}, \quad \ell_c = \tilde{h}_0, \tag{28}$$

where the characteristic velocity, u_c, is the Nusselt free-surface speed for the case when there is no gas flow above the film. The governing equation take the form

$$Re\,(u_t + uu_x + vu_y) = -p_x + u_{xx} + u_{yy} + 2, \tag{29a}$$

$$Re\,(v_t + uv_x + vv_y) = -p_y + v_{xx} + v_{yy} - 2\cot\theta, \tag{29b}$$

$$u_x + v_y = 0, \tag{29c}$$

where Re is the Reynolds number defined as

$$Re = \frac{\rho_\ell u_c \tilde{h}_0}{\mu_\ell}. \tag{30}$$

At the wall, $y = 0$, no-slip and no-penetration conditions are satisfied: $u = v = 0$. The kinematic condition and the tangential and normal stress balance conditions at the interface, $y = h(x,t) = 1 + \sum_{\substack{n=-\infty \\ n\neq 0}}^{\infty} h_n(t) e^{\mathrm{i}\alpha_n x}$, require

$$h_t + uh_x = v, \quad \text{at} \quad y = h(x,t), \tag{31a}$$

$$-\frac{1}{1+h_x^2}\left[2(u_x - v_y)h_x - (u_y + v_x)(1 - h_x^2)\right] = \hat{\tau}_w[h], \tag{31b}$$

$$p = \hat{P}_w[h] + \frac{2}{1+h_x^2}\left[u_x h_x^2 - (u_y + v_x)h_x + v_y\right] - \frac{Re\,We}{(1+h_x^2)^{3/2}}. \tag{31c}$$

In Eq. (31b) $\hat{\tau}_w[h]$ is the shear stress exerted by the gas on the interface given by

$$\hat{\tau}_w[h] = \frac{\tilde{h}_0}{\mu_l \tilde{u}_0}\tilde{\tau}_w[\tilde{h}] = \hat{\tau}_{w0} + \hat{\tau}_{w0\nu}\,\hat{\tau}_{w1}[h], \tag{32}$$

where

$$\hat{\tau}_{w0} = \frac{\tilde{h}_0 T_w \tau_{w0}}{\mu_l \tilde{u}_0}, \qquad \nu = \frac{\tilde{h}_0 \rho_g U_f^*}{\mu_g}, \qquad \hat{\tau}_{w1}[h] \equiv \sum_{\substack{n=-\infty \\ n\neq 0}}^{\infty} h_n \tau_{w1}(\alpha_n/\nu) \mathrm{e}^{\mathrm{i}\alpha_n x}. \tag{33}$$

Note that ν is the ratio of the length scales used to non-dimensionalize the liquid and the gas problems, respectively. In Eq. (31c) $\hat{P}_w[h]$ is the normal stress exerted by the gas on the interface that is given by

$$\widehat{P}_w[h] = \frac{h_0}{\mu_l \tilde{u}_0} \widetilde{P}_w[\tilde{h}] = \widehat{P}_0 + \hat{\tau}_{w0} \nu \widehat{P}_1[h], \tag{34}$$

with

$$\widehat{P}_0 = \hat{\tau}_{w0} P_0, \qquad \widehat{P}_1[h] \equiv \sum_{\substack{n=-\infty \\ n\neq 0}}^{\infty} h_n P_{w1}(\alpha_n/\nu) \mathrm{e}^{\mathrm{i}\alpha_n x}. \tag{35}$$

The dimensionless parameter We is the Weber number that signifies the ratio of surface tension forces to the inertial forces, and is defined as

$$We = \frac{\sigma}{\rho_\ell u_c^2 \sin\theta}. \tag{36}$$

Note that the Weber number, We, can further be expressed in terms of the Kapitza number, Ka, and the Reynolds number, Re, as follows

$$We = \frac{4Ka}{Re_0^{5/3} \sin^2\theta}, \tag{37}$$

where, $Ka = \sigma \rho_\ell^{1/3}/(g^{1/3}\mu_\ell^{4/3})$ depends on the properties of the liquid only, and $Re_0 = \rho_\ell^2 g \tilde{h}_0^3/\mu_\ell^2$ with $Re = (Re_0 \sin\theta)/2$. Note that for convenience we can write

$$\hat{\tau}_{w0} = \frac{2}{Re_0^{1/3} \sin\theta} \Theta \tau_{w0}, \qquad \nu = N Re_0^{1/3} \Theta^{1/2}, \tag{38}$$

where

$$\Theta = \frac{T_w}{\rho_l^{1/3} \mathrm{g}^{2/3} \mu_l^{2/3}}, \qquad N = \frac{\mu_l \rho_g^{1/2}}{\mu_g \rho_l^{1/2}}. \tag{39}$$

The parameter Θ controls the gas shear-stress strength, whilst the parameter N depends only on the densities and viscosities of the liquid and the gas.

4.1. IBL model

To develop a simplified model that captures the essential physics of the gas-liquid system considered here, we make use of the methodology developed by Ruyer-Quil and Manneville (1998, 2000) to model free-liquid films on an inclined plane. The starting point of this is the derivation of the first-order

boundary layer approximation. As in many thin-film settings, the problem can be substantially simplified, however, by utilizing the long-wave approximation, letting

$$\xi = x\epsilon; \quad \tau = t\epsilon; \quad v = w\epsilon, \tag{40}$$

where ϵ is the thin-film or long-wave parameter. Neglecting the higher-order inertia terms in the y-momentum equation, we have

$$p_y = -2\cot\theta + \mathcal{O}(\epsilon, \epsilon^2\, Re). \tag{41}$$

Considering only the leading-order contribution from the surface tension and gas flow in the normal stress balance equation, we obtain the pressure distribution from Eq. (41), which when substituted into the streamwise momentum equation results in

$$\epsilon Re\,[u_\tau + uu_\xi + wu_y] = -\epsilon\left(2\cot\theta h_\xi - \epsilon^2 Re\, We\, h_{\xi\xi\xi}\right) + u_{yy} + 2, \tag{42}$$

where $We = \mathcal{O}(\epsilon^{-2})$, and terms of $\mathcal{O}(\epsilon^2)$ and $\mathcal{O}(\epsilon^3 Re)$ are neglected. Equation (42) is accompanied by the no-slip condition at the bottom wall and the kinematic condition at the free surface:

$$h_\tau + q_\xi = 0, \tag{43}$$

where $q = \int_0^h u\, dy$ is the local flow rate. Finally, we have the tangential stress balance

$$u_y = \hat{\tau}_{w0} + \epsilon\bar{\nu}\hat{\tau}_{w1}[h] \quad \text{at} \quad y = h(\xi, \tau). \tag{44}$$

Equations (42)-(44) are the first-order boundary-layer equations for the gas-liquid problem. We further combine this first-order boundary-layer approximation with a weighted-residuals technique, in which the velocity component u is expanded in polynomial test functions so that the no-slip condition is automatically satisfied, and after incorporating the kinematic condition (43) and the tangential stress balance (44), is substituted into the x-component of the momentum equation to obtain the residual. Then a simple Galerkin projection with just one test function yields the following set of coupled partial differential equations for the interface thickness, and the local flow rate, which is written in the following form using variables t and x:

$$\begin{aligned} q_t = &-\frac{17}{7}\frac{q\,q_x}{h} + \frac{9}{7}\frac{q^2\,h_x}{h^2} - \frac{5}{2\,Re}\frac{q}{h^2} + \frac{5}{3\,Re}h - \frac{5\cot\theta}{3Re}hh_x + \frac{5\,We}{6}hh_{xxx} \\ &+ \hat{\tau}_{w0}\left(\frac{5}{4\,Re} - \frac{19\hat{\tau}_{w0}}{672}h^2h_x - \frac{19}{336}hq_x - \frac{5}{112}qh_x + \frac{5\,\nu}{4Re}\hat{\tau}_{w1}[h]\right), \end{aligned} \tag{45}$$

$$h_t + q_x = 0. \tag{46}$$

The terms in parentheses multiplying $\hat{\tau}_{w0}$ in Eq. (45) correspond to the influence of the turbulent gas flow. By setting $\hat{\tau}_{w0}$ to zero, we recover the first-order IBL approximation for a free-falling liquid film developed by Ruyer-Quil and Manneville (2000).

4.2. Linear stability analysis

A flat liquid film ($h = 1$) is a solution to the system of equations (45)-(46). To understand the stability of this solution to infinitesimal disturbances, we substitute $h = 1 + f$, $q = \frac{2}{3} + \frac{\hat{\tau}_{w0}}{2} + g$, where $|f| \ll 1$ and $|g| \ll 1$ in (45)-(46), and retaining only the first-order terms, gives

$$f_t + g_x = 0, \tag{47}$$

$$\begin{aligned} g_t = &-\frac{17}{7}\left(\frac{2}{3} + \frac{\hat{\tau}_{w0}}{2}\right) g_x + \frac{9}{7}\left(\frac{2}{3} + \frac{\hat{\tau}_{w0}}{2}\right)^2 f_x - \frac{5}{2Re}\left(g - \frac{4}{3}f - \hat{\tau}_{w0} f\right) \\ &+ \frac{5}{3Re} f - \frac{5\cot\theta}{3Re} f_x + \frac{5We}{6} f_{xxx} + \hat{\tau}_{w0}\left(-\frac{19}{672}\hat{\tau}_{w0} f_x - \frac{19}{336} g_x \right. \\ &\left. - \frac{5}{112}\left(\frac{2}{3} + \frac{\hat{\tau}_{w0}}{2}\right) f_x + \frac{5\,\nu}{4Re}\hat{\tau}_{w1}[f]\right). \end{aligned} \tag{48}$$

Looking for solutions in the form of normal modes, i.e., $(f, g) = (\bar{f}, \bar{g})\, \mathrm{e}^{s(k)t + \mathrm{i}kx}$, where $s(k)$ is the frequency and k is the wavenumber, from eqs. (47) and (48), we have the following dispersion relation

$$\begin{aligned} s^2(k) + &\frac{1}{336Re}\Big(840 + \mathrm{i}Re(544 + 427\hat{\tau}_{w0})k\Big) s(k) + \frac{5We}{6}k^4 \\ &+ \frac{1}{336Re}\Big(- Re(192 + 91\hat{\tau}_{w0}^2 + 278\hat{\tau}_{w0}) + 560\cot\theta\Big)k^2 \\ &+ \mathrm{i}\frac{5}{4Re}\left(4 + 2\hat{\tau}_{w0} + \nu\hat{\tau}_{w0}\tau_{w1}\left(\frac{k}{\nu}\right)\right)k = 0. \end{aligned} \tag{49}$$

When there is no gas flow, the flat film solution is stable for $Re < Re_c \equiv 5\cot\theta/4$, which is consistent with previous results (Benjamin (1957); Yih (1963)). But for $Re > Re_c$, we have a band of wavenumbers k for which the solution is unstable. Note that for the vertical setting ($\theta = \pi/2$) considered here in the computations that follow, the flat film solution becomes unstable when $Re = 0$. Fig. 3 shows the growth rate as a function of wavenumber for the most unstable eigenvalue and for the vertical configuration.

We can observe that the cocurrent turbulent gas flow is destabilizing in nature, as the growth rate is amplified (solid curve) when compared to the 'no-gas' situation (dashed curve). From Fig. 4, where we plot the phase velocity of the most amplified disturbance as a function of wavenumber, we see that the cocurrent gas flow increases the wave speed as expected.

[Figure 3 about here.]

[Figure 4 about here.]

5. Nonlinear waves

Travelling waves are known to exist for free-falling liquid films, and we expect to find such solutions in the presence of gas flow. To analyze such waves, we rewrite the equations obtained from the IBL model (Eqs. (45)-(46)) in a frame of reference moving with speed c and for simplicity we consider a vertical setting ($\cot\theta = 0$). We then have

$$-ch_x + q_x = 0, \tag{50a}$$

$$\begin{aligned} -cq_x = &-\frac{17}{7}\frac{q\,q_x}{h} + \frac{9}{7}\frac{q^2\,h_x}{h^2} - \frac{5}{2\,Re}\frac{q}{h^2} + \frac{5}{3\,Re}h \\ &+\frac{5\,We}{6}hh_{xxx} + \hat{\tau}_{w0}\left(\frac{5}{4\,Re} - \frac{19\hat{\tau}_{w0}}{672}h^2h_x\right. \\ &\left.-\frac{19}{336}hq_x - \frac{5}{112}qh_x + \frac{5\nu}{4Re}\hat{\tau}_{w1}[h]\right). \end{aligned} \tag{50b}$$

We have retained the same independent variable 'x' for the moving coordinate for convenience. Here, we focus only on fast waves (traveling faster than infinitesimally small waves), in particular on the γ_2 family of periodic solutions for free-falling films, in terms of the classification of permanent waves given by Chang and Demekhin (2002). The solitary-wave limit of such waves corresponds to a single-hump solitary wave and is represented by a homoclinic orbit in the phase space of the corresponding dynamical system (Balmforth (1995); Chang and Demekhin (2002); Kalliadasis et al. (2011)). Single-hump solitary waves, are characterized by a single-hump/elevation followed by rapidly decaying capillary ripples at the wavefront, and travel faster than the small-amplitude waves. We consider waves in two different settings – in one, the film thickness is fixed to unity at infinity, i.e., $h \to 1$ as $x \to \pm\infty$ (this corresponds to solitary waves), and in another one, we fix the mass flow rate under a wave to a constant, which is accomplished by taking $1/(2\mathrm{W})\int_{-W}^{W} h\,dx = 1$, where W is taken to be the half-length of the domain of integration (this corresponds to periodic travelling waves). As a first step, we integrate Eq. (50a) once to obtain

$$-ch + q = C_0, \tag{51}$$

where, C_0 is the constant of integration.

5.1. Solitary waves ($h = 1$, as $x \to \pm\infty$)

When $h \to 1$ as $x \to \pm\infty$, we have $q \to 2/3 + \hat{\tau}_{w0}/2$. Therefore, in Eq. (51) $C_0 = -c + 2/3 + \hat{\tau}_{w0}/2$, and we can eliminate q in Eq. (50b) by substituting $q = c(h-1) + 2/3 + \hat{\tau}_{w0}/2$ to obtain

$$\begin{aligned} h^3 h_{xxx} + \frac{1}{35We}\Big(-6c^2 h(h+1) + 4ch + 6(3c-2)^2\Big) h_x \\ + \frac{\hat{\tau}_{w0}}{280We}\Big(24ch - 432c + 288 - 34ch^3 + 15ch^2 - 10h^2\Big) h_x \\ + \frac{\hat{\tau}_{w0}^2}{560We}\left(216 - 19h^4 - 15h^2\right) h_x - \frac{3}{WeRe}\left(c(h-1) + \frac{2}{3}\right) \\ + \frac{3\hat{\tau}_{w0}}{2WeRe}\Big(h^2\left(1 + \nu\hat{\tau}_{w1}[h]\right) - 1\Big) + \frac{2}{WeRe}h^3 = 0. \end{aligned} \tag{52}$$

To solve for the additional variable in the form of the wave velocity c, we take the derivative of the interface h to be vanishing at the midpoint of the domain, $h_x|_{x=0} = 0$. This system of equations is solved numerically on a periodic domain with spectral discretization along the spatial direction. We adopt helium(g)-methanol(l) as working fluids in our study, which were considered by Zapke and Kröger (2000a,b) in their counter-current gas-liquid flow experiments. The physical properties of the fluids are as follows:

$$\rho_g = 0.165\ \mathrm{kg/m^3}, \quad \mu_g = 2 \times 10^{-5}\ \mathrm{Pa\ s}, \tag{53a}$$

$$\rho_\ell = 791\ \mathrm{kg/m^3}, \quad \mu_\ell = 5.75 \times 10^{-4}\ \mathrm{Pa\ s}, \quad \sigma = 22 \times 10^{-3}\ \mathrm{N/m}, \tag{53b}$$

which in terms of dimensionless numbers are given by

$$Ka = 1988.5, \quad N = 0.4. \tag{54}$$

To analyze the dependence of the wave velocity c on the liquid Reynolds number Re, we solve Eq. (52) along with the first-derivative condition mentioned above implementing Keller's pseudo-arclength continuation algorithm (Keller (1977)).

5.1.1. Continuation along Re

[Figure 5 about here.]

Fig. 5 shows the dependence of the wave speed c on the liquid Reynolds number Re for various values of the gas shear parameter Θ. The solitary waves are computed on a sufficiently long periodic domain with a period of 900 dimensionless units. For a given Θ, it can be observed that the wave speed c increases with Re before coming to a near saturation or exhibiting turning point at higher

Re. We note that the curve obtained for $\Theta = 0$ is qualitatively similar to that obtained by Demekhin et al. (2010) for water-air as working fluids in a falling film problem. For smaller Re, where the flow is governed by viscous drag and gravity, c increases rapidly, and for larger Re where inertia becomes important, we have a plateau-like region for c.

As we increase Θ, the wave speed increases for a given Re. This is only to be expected as the gas flowing in the same direction as the liquid would only increase the speed of the wave further. At higher speeds of the solitary wave, there is a rise in the amplitude of the hump followed by more pronounced capillary ripples at the wave front. In this regime, the shear force due to the co-flowing gas flow becomes important in addition to the viscous drag, gravity, inertia and surface tension. It is important to note that the solitary wave attains a higher speed for larger Θ, even for moderately small values of the liquid Reynolds number Re. As Re increases further, the capillary waves become appreciably large and a large domain is required is compute the solitary waves. Thus, the presence of the turning points shown in Fig. 6 may be attributed, at least partly, to the domain size.

[Figure 6 about here.]

[Figure 7 about here.]

[Figure 8 about here.]

Some of the other characteristics of the solitary waves, namely the maximum and minimum of the free surface, $\max(h)$ and $\min(h)$, are plotted as functions of Re for various values of Θ in Figs. 7 and 8, respectively. In the absence of turbulent gas flow ($\Theta = 0$), both the maximum and the minimum of the wave height tend to unity, as we approach $Re = 0$ implying that h approaches unity. For nonzero Θ, the maximum increases with increasing Re (implying the increase in the height of the hump) whereas the minimum decreases with increase in Re. The minimum of h comes from the first dimple in the capillary ripples following the hump.

From the solitary-wave profiles shown in Fig. 9 for various values of the gas shear parameter Θ at $Re = 5$, we can observe the increase in the wave height for increasing Θ, and the capillary ripples become more pronounced.

[Figure 9 about here.]

5.1.2. Continuation along Θ

We have also performed numerical continuation along the gas shear parameter Θ for two values of the liquid Reynolds number, $Re = 3, 5$. The continuation results shown in Fig. 10 indicate that

c indeed increases with Θ, which is again consistent with our previous observations. The numerical values for the wave speed obtained from both continuation approaches show excellent agreement.

[Figure 10 about here.]

5.2. Travelling waves

Instead of fixing the thickness of the flat film to unity, we now fix the volume under the wave to a constant value – that could be realized in experimental studies. In this fixed-volume setting, we eliminate q in Eq. (50b) by substituting $q = C_0 + ch$ to obtain

$$\begin{aligned} h^3 h_{xxx} + \frac{6}{5We}\Bigg(& c^2h^2 - \frac{17}{7}\left(C_0 + ch\right)ch + \frac{9}{7}\left(C_0 + ch\right)^2 \\ & - \frac{19}{672}\hat{\tau}_{w0}^2 h^4 - \frac{19}{336}\hat{\tau}_{w0} ch^3 - \frac{5}{112}\hat{\tau}_{w0}h^2\left(C_0 + ch\right)\Bigg)h_x \\ + \frac{2}{WeRe}h^3 - \frac{3}{WeRe}\left(C_0 + ch - \frac{\hat{\tau}_{w0}}{2}h^2\Big(1 + \nu\hat{\tau}_{w1}[h]\Big)\right) = 0. \end{aligned} \tag{55}$$

As before, we impose the condition $h_x|_{x=0} = 0$. Also, since the additional unknown C_0 is introduced, we impose an additional integral condition which is the equation for the constant mass under the wave, i.e., $1/(2\mathrm{W})\int_{-W}^{W} h\,dx = 1$. Here, the period of integration is taken to be 600 dimensionless units. We solve Eq. (55) together with the derivative and integral conditions using a spectral method.

5.2.1. Continuation along Re

As in the previous section, we carry out continuation along Re by fixing Θ. Fig. 11 shows the variation of c as a function of Re, obtained from numerical continuation. Though there is a general trend of c increasing as Re increases, we can identify a number of differences compared to the case with the constant film thickness in the far field. In comparison, the increase of c with Re appears to be slower, but there is also a slow and steady decrease in c beyond some Re (for $\Theta = 1.5$). This is due to the fact that fixing the volume under a wave results in a decrease in the height of the flat film region as Re increases (hence a more constrained increase in the wave amplitude), and as the wave speed is proportional to its amplitude, the speed has to decrease. In other words, solitary waves travel faster than periodic travelling waves.

In Fig. 14, we plot the profiles of the free surface which also reveal the decrease in the thickness of the flat film sufficiently far from the hump. Furthermore, the maximum and the minimum of the wave profiles, plotted respectively in Figs. 12 and 13, indicate that the amplitude is smaller when compared with the case in which the flat film thickness is fixed to unity in the far field.

[Figure 11 about here.]

[Figure 12 about here.]

[Figure 13 about here.]

[Figure 14 about here.]

The variation of the wave velocity c with the gas flow parameter Θ shown in Fig. 15, indicates that c increases as Θ increases but at a slightly slower rate.

[Figure 15 about here.]

It should be noted that our time-dependent computations of the IBL model on a periodic domain of dimensionless length 600 show that the number of single-hump waves arising in the computational domain depends on the chosen initial conditions. For instance, in Sect. 6 we discuss the case when the initial conditions are small-amplitude sinusoidal disturbances of the flat-film solution, and the interface evolves into a superposition of four single-hump waves of approximately the same shape. Therefore, to make a comparison with our time-dependent computations presented in Sect. 6, it turns out it is more appropriate to compute travelling waves on a smaller domain of length 150 dimensionless units. The dependence of c on Re shown in Fig. 16 reveals a non-monotonic behavior, particularly with increasing gas shear ($\Theta = 1.5$), also exhibiting multiple solutions. Such a behavior can be attributed to the fact that the waves are not isolated due to the smallness of the domain, thereby showing tail interactions. The comparison between the steady travelling-wave profiles and the profiles obtained in the time-dependent computations is discussed in Sect. 6.

[Figure 16 about here.]

6. Time-dependent computation

To understand the spatiotemporal evolution of the gas-liquid interface under the influence of turbulent gas flow, we need to solve Eqs. (45)-(46) as an initial value problem. This is carried out numerically using a Fourier pseudo-spectral representation of the spatial derivatives and an adaptive stepping in time. To investigate the influence of gas flow on the dynamics of the liquid film, we increase Θ in steps of 0.5 starting from 0, for every 1000 dimensionless time units, during which we track the spatiotemporal evolution of h and q by solving Eqs. (45)-(46). We choose the initial condition of the

interface to be a flat film ($h = 1$), superimposed with a sinusoidal disturbance of amplitude 0.05 in the absence of turbulent gas. The liquid Reynolds number is fixed to be $Re = 5$. The equations are integrated on a periodic domain $[-300, 300]$ for sufficiently long time, say till $t \approx 10000$. The interface attains a nearly steady traveling-wave state, whereby the unsteadiness is attributed to the interaction between individual waves. The corresponding spatiotemporal profile for a free-falling liquid film when the wave profile attains such a state is shown as a space-time plot in Fig. 17 (for $t = 9000 - 10000$). The darker regions correspond to larger h, whereas the brighter regions correspond to smaller h, with the shading done following the color bar in Fig. 17. A snapshot of the actual profile is shown in Fig. 18a. The lines in the space-time plot show the trace of peaks/humps of the traveling waves, and their inverse slopes correspond to the wave speed. The solution for the film thickness h and the flow rate q at $t = 10000$ is used as the initial condition, when we introduce the gas flow that is turbulent in nature.

To introduce the gas flow, we set $\Theta = 0.5$ corresponding to the friction velocity $U_f^* = 0.94\,\mathrm{m/s}$. From the space-time plot shown in Fig. 17 (for $t = 10000 - 11000$), we observe that the lines become more horizontal than for the free-falling case, implying that the waves travel faster with higher amplitudes. This is further confirmed by the interface profiles shown in Fig. 18b. We use the solution (h, q) at $t = 11000$ as an initial condition when we further increase the gas shear to $\Theta = 1.0$ with the corresponding friction velocity $U_f^* = 1.33\,\mathrm{m/s}$. We can observe the increase in the wave velocity and the height by noting that the lines become more horizontal Fig. 17 (for $t = 11000 - 12000$), and darker. The interfacial wave profiles shown in Fig. 18c clearly indicate that their amplitudes are larger when compared with the previous cases, $\Theta = 0, 0.5$. The increase of the speed and amplitude of the waves is again observed as we increase Θ further to 1.5 corresponding to $U_f^* = 1.63\,\mathrm{m/s}$ (shown in Fig. 17 for $t = 12000 - 13000$ and the interface profiles in Fig. 18d), until the flow increases to a point where the long-wave assumption is no longer applicable. At this stage, the full Navier-Stokes equations for the gas and the liquid need to be used to describe the flow behavior.

It can be observed that there are four waves in the computational domain of size 600 dimensionless units, chosen for the time-dependent computations. So it turns out more appropriate to compare the results of the time-dependent computations with the numerical-continuation results for the fixed-volume case on the domain of length 150 dimensionless units. A comparison of the wave velocities obtained from both computations shows very good agreement, with the difference being smaller than 1%. This difference could be attributed to the presence of interactions (attractions–repulsions) between the waves in the entire domain in the time-dependent computations. Such interactions are not taken

into account in our numerical-continuation computations. The wave profiles obtained from both the time-dependent simulations and the numerical-continuation computations ($W = 75$) also show very good agreement, as can be seen in Fig. 19.

[Figure 17 about here.]

[Figure 18 about here.]

[Figure 19 about here.]

7. Conclusion

We have analyzed the dynamics of a thin liquid layer flowing under gravity down a planar vertical substrate in the presence of a co-flowing turbulent gas. The gas and liquid problems were solved separately by combining the fact that the viscosity of the gas is much smaller than that of the liquid and the following assumptions: the velocity in the liquid layer is much smaller than the mean velocity in the gas layer and that the turbulent fluctuations in the gas flowing over the liquid film decay in the same way as those in the gas flowing over a rigid wall.

The perturbations to the interfacial shear stress computed by solving the gas problem are used in the interfacial boundary conditions to solve the liquid problem. To describe the dynamics of the liquid layer, we have derived an integral-boundary-layer (IBL) model. We used this model to analyze the effect of the gas flow on single-hump solitary and travelling waves (γ_2 type), which are commonly observed in the falling film setting. For solitary waves we require that the film thickness approaches a given constant value in the far field, while for periodic travelling waves we require that the volume is kept fixed in one period. By taking helium and methanol as working fluids, we have computed such waves using Keller's pseudo-arclength continuation algorithm.

The dependence of the wave velocity on the liquid Reynolds number and the gas flow is analyzed. It is found that the wave velocity increases with the liquid Reynolds number as well as the gas shear. This is markedly different from the counter-current setting, where, for a given liquid Reynolds number, the wave velocity decreases with increasing gas shear before changing direction at the flooding point. We have also compared our numerical continuation results with time-dependent computations of the IBL model, showing very good agreement, with just a small mismatch in the wave velocity which can be attributed to the interaction (attraction and repulsion) between neighboring waves in the computational domain.

It is noteworthy that in the existing literature, experimental studies were conducted at high liquid Reynolds numbers (e.g. Lioumbas et al. (2005, 2006, 2009)) and hence no direct comparisons between these studies and the present one valid for low liquid Reynolds number can be made. However, it is hoped that our study can motivate experimental studies on this subject as well as additional theoretical studies in other settings where gas-liquid flows are pertinent. For instance, co-current gas-liquid flows also find applicability in the generation of droplets (Lasheras and Hopfinger, 2000), wherein the shearing action of a co-flowing high-speed gas stream over a slow-flowing liquid jet results in the formation of droplets of different sizes.

8. Acknowledgements

We are grateful to Dr. Benoit Scheid for useful comments and suggestions. We acknowledge financial support via the European Framework 7 via Grant No. 214919 (Multiflow) and the Engineering and Physical Sciences Research Council of the UK via Grant No. EP/J001740/1.

References

Alekseenko, S., Antipin, V., Cherdantsev, A., Kharlamov, S., Markovich, D., 2009. Two-wave structure of liquid film and wave interrelation in annular gas-liquid flow with and without entrainment. Phys. Fluids 21, 061701.

Alekseenko, S.V., Nakoriakov, V.E., Pokusaev, B.G., 1994. Wave Flow of Liquid Films. Begell House, New York.

Balmforth, N.J., 1995. Solitary waves and homoclinic orbits. Ann. Rev. Fluid Mech. 27, 335–373.

Benjamin, T.B., 1957. Wave formation in laminar flow down an inclined plane. J. Fluid Mech. 2, 554–574.

Benjamin, T.B., 1959. Shearing flow over a wavy boundary. J. Fluid Mech. 6, 161–205.

Chang, H.C., Demekhin, E.A., 2002. Complex wave dynamics on thin films. Elsevier.

Chang, H.C., Demekhin, E.A., Kalaidin, E.N., 1995. Interaction dynamics of solitary waves on a falling film. J. Fluid Mech. 294, 123–154.

Cohen, L.S., Hanratty, T.J., 1965. Generation of waves in the concurrent flow of air and a liquid. AIChE J. 11, 138–144.

Craik, A.D.D., 1966. Wind generated waves in thin liquid films. J. Fluid Mech. 26, 369 – 392.

Demekhin, E.A., 1981. Nonlinear waves in a liquid film entrained by a turbulent gas stream. Fluid Dyn. 16, 188–193.

Demekhin, E.A., Kalaidin, E.N., Kalliadasis, S., Vlaskin, S.Y., 2010. Three-dimensional localized coherent structures of surface turbulence: Model validation with experiments and further computations. Phys. Rev. E 82, 036322.

Frank, A.M., 2006. Shear driven solitary waves on a liquid film. Phys. Rev. E 74, 065301.

Hanratty, T.J., Engen, J.M., 1957. Interaction between a turbulent air stream and a moving water surface. AIChE J. 3, 299–304.

Jurman, L.A., McCready, M.J., 1989. Study of waves on thin liquid films sheared by turbulent gas flows. Phys. Fluids A 1, 522–536.

Kalliadasis, S., Demekhin, E.A., Ruyer-Quil, C., Velarde, M.G., 2003. Thermocapillary instability and wave formation on a film falling down a uniformly heated plane. J. Fluid Mech. 492, 303–338.

Kalliadasis, S., Ruyer-Quil, C., Scheid, B., Velarde, M.G., 2011. Falling liquid films. Springer.

Kapitza, P.L., 1965. Collected Papers of P. L. Kapitza. Pergamon (Oxford). pp. 662–689.

Keller, H.B., 1977. Numerical solution of bifurcation and nonlinear eigenvalue problems. Academic Press.

Lasheras, J.C., Hopfinger, E.J., 2000. Liquid jet instability and atomization in a coaxial gas stream. Ann. Rev. Fluid Mech. 32, 275 – 308.

Lioumbas, J., Kolimenos, C., Paras, S., 2009. Liquid layer characteristics in gas-liquid flow in slightly inclined pipes: Effect of non-ionic surfactant additives. Chem. Engng Sci. 64, 5162 – 5172.

Lioumbas, J., Mouza, A., Paras, S., 2006. Effect of surfactant additives on co-current gas-liquid downflow. Chem. Engng Sci. 61, 4605 – 4616.

Lioumbas, J., Paras, S., Karabelas, A., 2005. Co-current stratified gas-liquid downflow – Influence of the liquid flow field on interfacial structure. Int. J. Multiphase Flow 31, 869 – 896.

Liu, J., Gollub, J.P., 1994. Solitary wave dynamics of film flows. Phys. Fluids 6, 1702–1712.

Malamataris, N.A., Balakotaiah, V., 2008. Flow structure underneath the large amplitude waves of a vertically falling film. AIChE J 54, 1725 –1740.

Miles, J.W., 1957. On generation of surface waves by shear flows. J. Fluid Mech. 3, 185 – 204.

Peng, C.A., Jurman, L.A., McCready, M.J., 1991. Formation of solitary waves on gas-sheared liquid layers. Int. J. Multiphase Flow 17, 767–782.

Pereira, A., Kalliadasis, S., 2008. Dynamics of a falling film with solutal marangoni effect. Phys. Rev. E 78, 036312.

Ruyer-Quil, C., Manneville, P., 1998. Modeling film flows down inclined planes. Eur. Phys. J. B 6, 277–292.

Ruyer-Quil, C., Manneville, P., 2000. Improved modeling of flows down inclined planes. Eur. Phys. J. B 15, 357–369.

Scheid, B., Ruyer-Quil, C., Kalliadasis, S., Velarde, M.G., Zeytounian, R.K., 2005a. Thermocapillary long waves in a liquid film flow. Part 2. Linear stability and nonlinear waves. J. Fluid Mech. 538, 223–244.

Scheid, B., Ruyer-Quil, C., Thiele, U., Kabov, O.A., Legros, J.C., Colinet, P., 2005b. Validity domain of the Benney equation including the Marangoni effect for closed and open flows. J. Fluid Mech. 527, 303–335.

Schlichting, H., 2000. Boundary-Layer Theory. Springer.

Thorsness, C., Morrisroe, P., Hanratty, T., 1978. A comparison of linear theory with measurements of the variation of shear stress along a solid wave. Chem. Engng Sci. 33, 579 – 592.

Trevelyan, P., Pereira, A., Kalliadasis, S., 2012. Dynamics of a reactive thin film. Math. Model. Nat. Phenom. 7, 99–145.

Trevelyan, P.M.J., Kalliadasis, S., 2004. Dynamics of a reactive falling film at large Péclet numbers. II. Nonlinear waves far from criticality: Integral-boundary-layer approximation. Phys. Fluids 16, 3209–3226.

Trifonov, Y.Y., 2010. Counter-current gas-liquid wavy film flow between the vertical plates analyzed using the Navier-Stokes equations. AIChE J. 56, 1975–1987.

Tseluiko, D., Kalliadasis, S., 2011. Nonlinear waves in counter-current gas-liquid film flow. J. Fluid Mech. 673, 19–59.

Van Driest, E.R., 1956. On turbulent flow near a wall. J. Aerospace Sci. 23, 1007–1011.

Vlachogiannis, M., Bontozoglou, V., 2001. Observations of solitary wave dynamics of film flows. J. Fluid Mech. 435, 191–215.

Woodmansee, D.E., Hanratty, T.J., 1969. Mechanism for the removal of droplets from a liquid surface by a parallel air flow. Chem. Engng Sci. 24, 299 – 307.

Yih, C., 1963. Stability of a liquid flow down an inclined plane. Phys. Fluids 6, 321–334.

Zapke, A., Kröger, D., 2000a. Countercurrent gas-liquid flow in inclined and vertical ducts — I: Flow patterns, pressure drop characteristics and flooding. Int. J. Multiphase Flow 26, 1439 – 1455.

Zapke, A., Kröger, D., 2000b. Countercurrent gas-liquid flow in inclined and vertical ducts — II: The validity of the Froude–Ohnesorge number correlation for flooding. Int. J. Multiphase Flow 26, 1457 – 1468.

Zilker, D.P., Cook, G.W., Hanratty, T.J., 1977. Influence of the amplitude of a solid wavy wall on a turbulent flow. Part 1. Non-separated flows. J. Fluid Mech. 82, 29–51.

List of Figures

1 Schematic of the co-current gas liquid flow problem in an inclined channel. 27
2 Base-state velocity profile. 28
3 Dependence of the growth rate on the wavenumber for $Re = 5.0$, $\theta = \pi/2$, $Ka = 1988.5$, $N = 0.4$, $\Theta = 0$ (dashed curve) and $\Theta = 0.5$ (solid curve). 29
4 Dependence of the phase velocity on the wavenumber for $Re = 5.0$, $\theta = \pi/2$, $Ka = 1988.5$, $N = 0.4$, $\Theta = 0$ (dashed curve) and $\Theta = 0.5$ (solid curve). 30
5 Dependence of the solitary-wave speed c on the Reynolds number Re for various values of gas shear parameter Θ, with $\theta = \pi/2$, $Ka = 1988.5$ and $N = 0.4$. 31
6 Dependence of the solitary-wave speed c on the Reynolds number Re, showing turning points for $\Theta = 1.5$, $\theta = \pi/2$, $Ka = 1988.5$ and $N = 0.4$. 32
7 Dependence of the maximum height of the solitary wave on the Reynolds number Re for various values of gas shear parameter Θ, with $\theta = \pi/2$, $Ka = 1988.5$ and $N = 0.4$. 33
8 Dependence of the minimum height of the solitary wave on the Reynolds number Re for various values of gas shear parameter Θ, with $\theta = \pi/2$, $Ka = 1988.5$ and $N = 0.4$. 34
9 Solitary-wave profiles for various values of the gas shear parameter Θ at $Re = 5.0$, $\theta = \pi/2$, $Ka = 1988.5$ and $N = 0.4$. Only a part of the domain is shown for the sake of clarity. 35
10 Dependence of the solitary-wave speed c on the gas shear parameter Θ for $Re = 3.0$ and $Re = 5.0$, with $\theta = \pi/2$, $Ka = 1988.5$ and $N = 0.4$. 36
11 Dependence of the travelling-wave speed c on the Reynolds number Re for various values of gas shear parameter Θ (fixed volume condition), with $\theta = \pi/2$, $Ka = 1988.5$ and $N = 0.4$. 37
12 Dependence of the maximum height of the travelling wave on the Reynolds number Re for various values of gas shear parameter Θ (fixed volume condition), with $\theta = \pi/2$, $Ka = 1988.5$ and $N = 0.4$. 38
13 Dependence of the minimum height of the travelling wave on the Reynolds number Re for various values of the gas shear parameter Θ (fixed volume condition), with $\theta = \pi/2$, $Ka = 1988.5$ and $N = 0.4$. 39
14 Travelling-wave profiles for various values of the gas shear parameter Θ at $Re = 5.0$ (fixed volume condition), with $\theta = \pi/2$, $Ka = 1988.5$ and $N = 0.4$. Only a part of the domain is shown for the sake of clarity. 40
15 Dependence of the travelling-wave speed c on the gas shear parameter (Θ) for $Re = 3.0, 5.0$, with $\theta = \pi/2$, $Ka = 1988.5$ and $N = 0.4$. 41
16 Dependence of the travelling-wave speed c on the Reynolds number Re for various values of gas shear parameter Θ (fixed volume condition) on a smaller domain ($W = 75$), with $\theta = \pi/2$, $Ka = 1988.5$ and $N = 0.4$. 42
17 Space-time plot of the gas-liquid interface at $Re = 5$ for various strengths of the gas shear, with $\theta = \pi/2$, $Ka = 1988.5$ and $N = 0.4$. Brighter regions correspond to small amplitudes, and darker regions correspond to large amplitudes. Ripples can be seen clearly when the figure is zoomed in. 43
18 Time evolution of the gas-liquid interface, for $\Theta = 0, 0.5, 1.0$ and 1.5, or, equivalently, U_f^*=0, 0.94, 1.33 and 1.63 m/s, with $\theta = \pi/2$, $Ka = 1988.5$ and $N = 0.4$. 44

19 Comparison of the wave profiles obtained by time-dependent computations on the periodic domain of dimensionless length 600 with the profiles of steady travelling waves obtained by continuation on the domain of dimensionless length 150, for various values of the gas shear parameter Θ at $Re = 5.0$, with $\theta = \pi/2$, $Ka = 1988.5$ and $N = 0.4$. The solid curves correspond to steady travelling waves obtained from continuation, whereas the open circles correspond to time-dependent simulations. Note that for the time-dependent simulations there are four waves in the domain and just one of them is selected and shown in each of the panels. 45

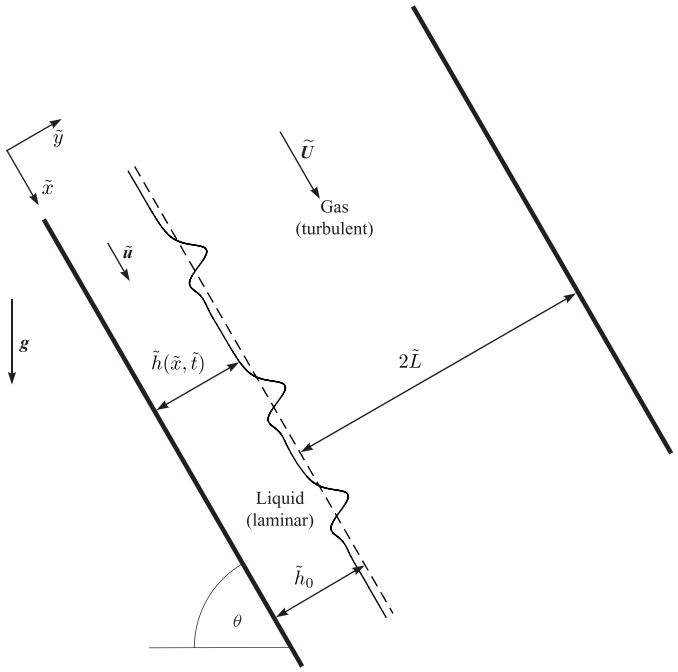


Figure 1: Schematic of the co-current gas liquid flow problem in an inclined channel.

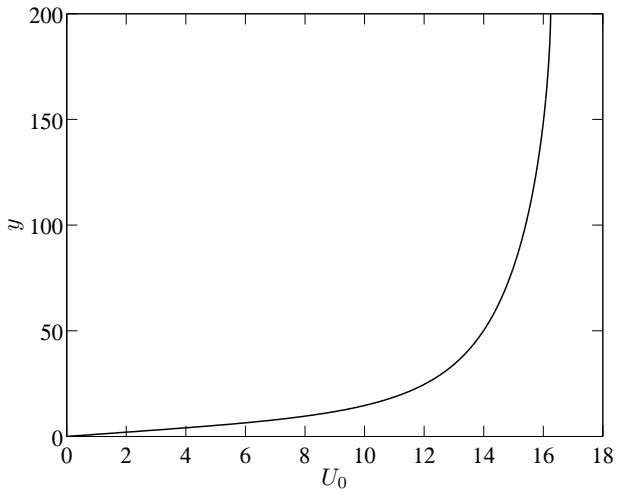


Figure 2: Base-state velocity profile.

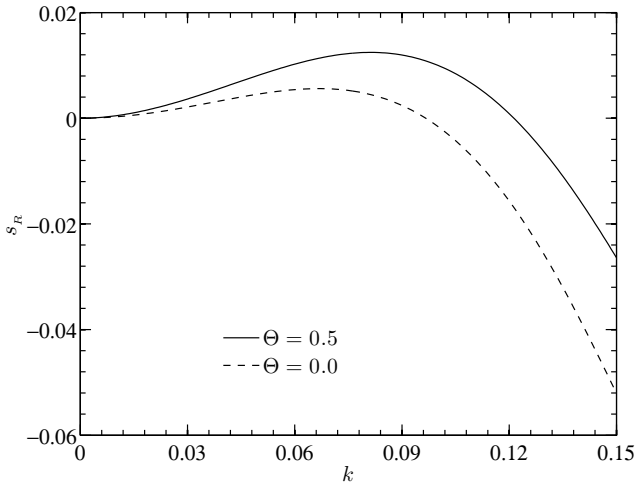


Figure 3: Dependence of the growth rate on the wavenumber for $Re = 5.0$, $\theta = \pi/2$, $Ka = 1988.5$, $N = 0.4$, $\Theta = 0$ (dashed curve) and $\Theta = 0.5$ (solid curve).

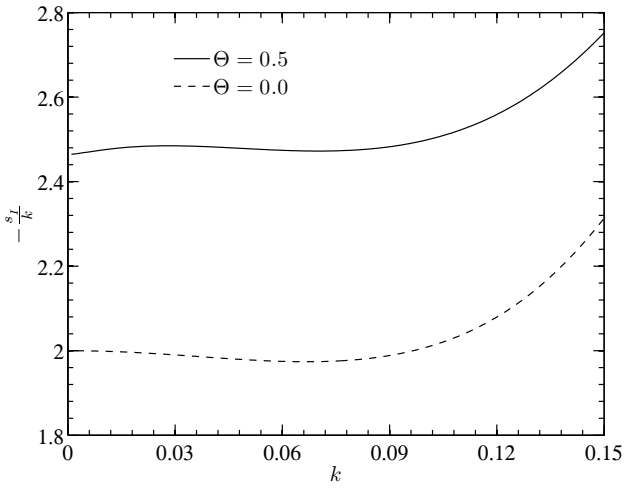


Figure 4: Dependence of the phase velocity on the wavenumber for $Re = 5.0$, $\theta = \pi/2$, $Ka = 1988.5$, $N = 0.4$, $\Theta = 0$ (dashed curve) and $\Theta = 0.5$ (solid curve).

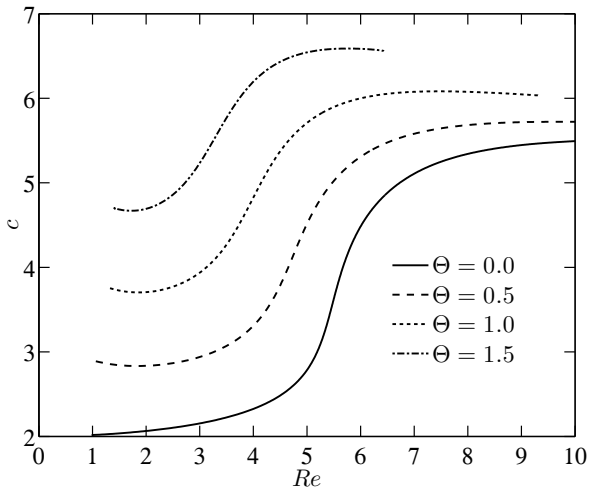


Figure 5: Dependence of the solitary-wave speed c on the Reynolds number Re for various values of gas shear parameter Θ, with $\theta = \pi/2$, $Ka = 1988.5$ and $N = 0.4$.

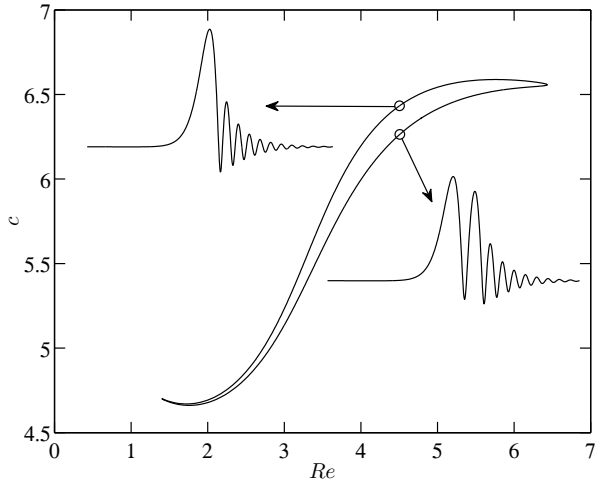


Figure 6: Dependence of the solitary-wave speed c on the Reynolds number Re, showing turning points for $\Theta = 1.5$, $\theta = \pi/2$, $Ka = 1988.5$ and $N = 0.4$.

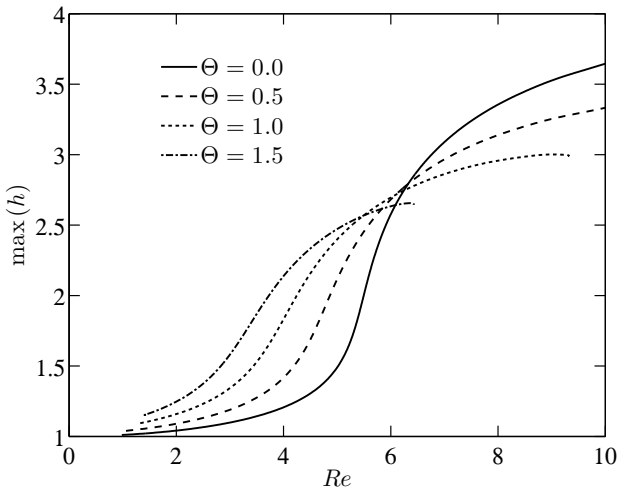


Figure 7: Dependence of the maximum height of the solitary wave on the Reynolds number Re for various values of gas shear parameter Θ, with $\theta = \pi/2$, $Ka = 1988.5$ and $N = 0.4$.

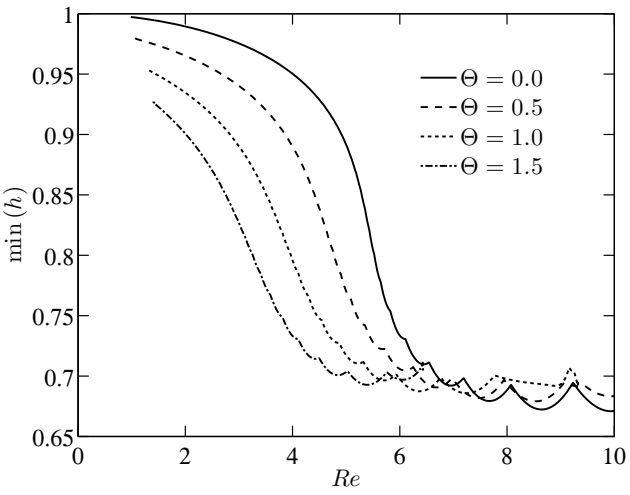


Figure 8: Dependence of the minimum height of the solitary wave on the Reynolds number Re for various values of gas shear parameter Θ, with $\theta = \pi/2$, $Ka = 1988.5$ and $N = 0.4$.

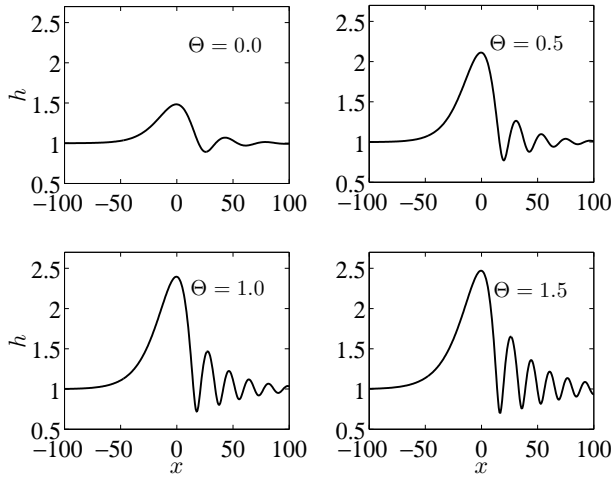


Figure 9: Solitary-wave profiles for various values of the gas shear parameter Θ at $Re = 5.0$, $\theta = \pi/2$, $Ka = 1988.5$ and $N = 0.4$. Only a part of the domain is shown for the sake of clarity.

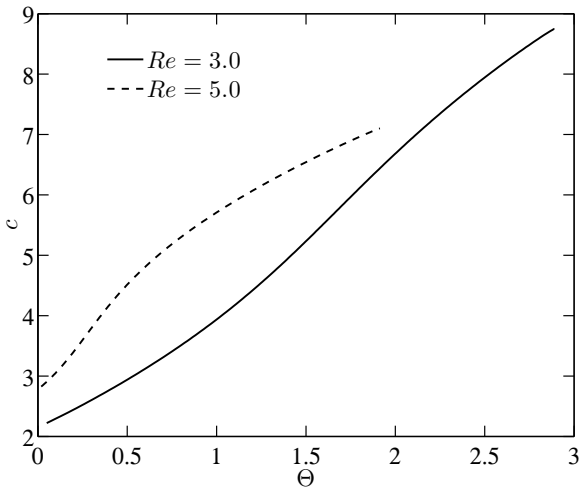


Figure 10: Dependence of the solitary-wave speed c on the gas shear parameter Θ for $Re = 3.0$ and $Re = 5.0$, with $\theta = \pi/2$, $Ka = 1988.5$ and $N = 0.4$.

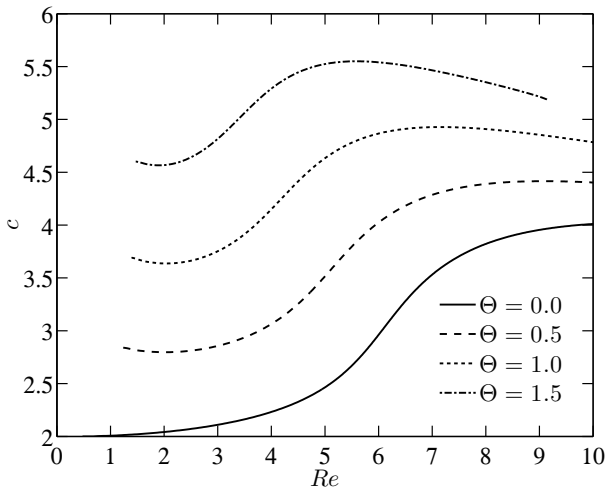


Figure 11: Dependence of the travelling-wave speed c on the Reynolds number Re for various values of gas shear parameter Θ (fixed volume condition), with $\theta = \pi/2$, $Ka = 1988.5$ and $N = 0.4$.

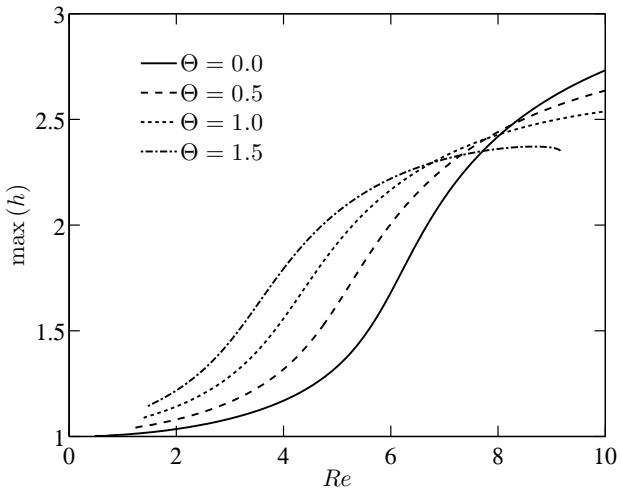


Figure 12: Dependence of the maximum height of the travelling wave on the Reynolds number Re for various values of gas shear parameter Θ (fixed volume condition), with $\theta = \pi/2$, $Ka = 1988.5$ and $N = 0.4$.

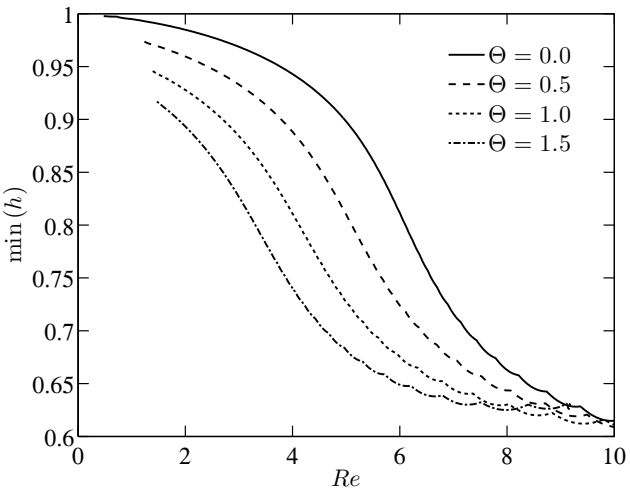


Figure 13: Dependence of the minimum height of the travelling wave on the Reynolds number Re for various values of the gas shear parameter Θ (fixed volume condition), with $\theta = \pi/2$, $Ka = 1988.5$ and $N = 0.4$.

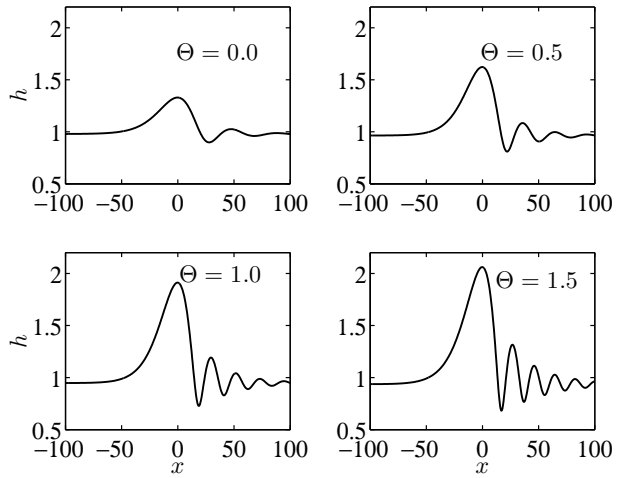


Figure 14: Travelling-wave profiles for various values of the gas shear parameter Θ at $Re = 5.0$ (fixed volume condition), with $\theta = \pi/2$, $Ka = 1988.5$ and $N = 0.4$. Only a part of the domain is shown for the sake of clarity.

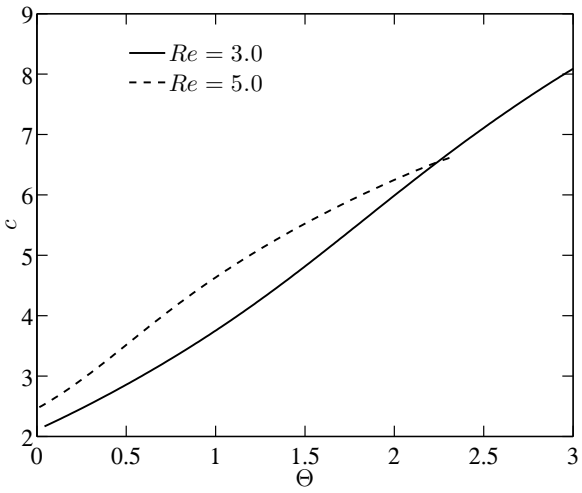


Figure 15: Dependence of the travelling-wave speed c on the gas shear parameter (Θ) for $Re = 3.0, 5.0$, with $\theta = \pi/2$, $Ka = 1988.5$ and $N = 0.4$.

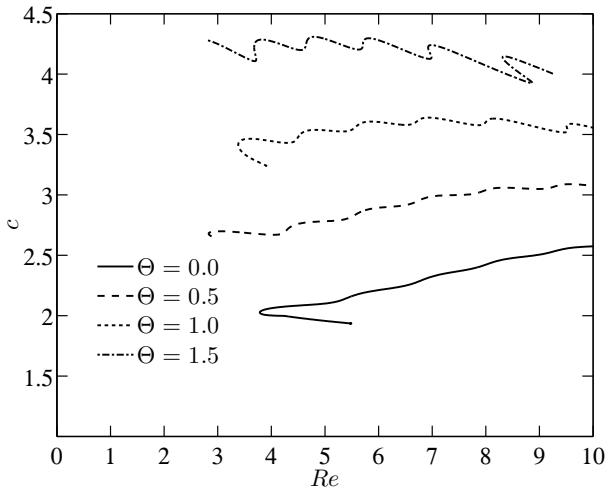


Figure 16: Dependence of the travelling-wave speed c on the Reynolds number Re for various values of gas shear parameter Θ (fixed volume condition) on a smaller domain ($W = 75$), with $\theta = \pi/2$, $Ka = 1988.5$ and $N = 0.4$.

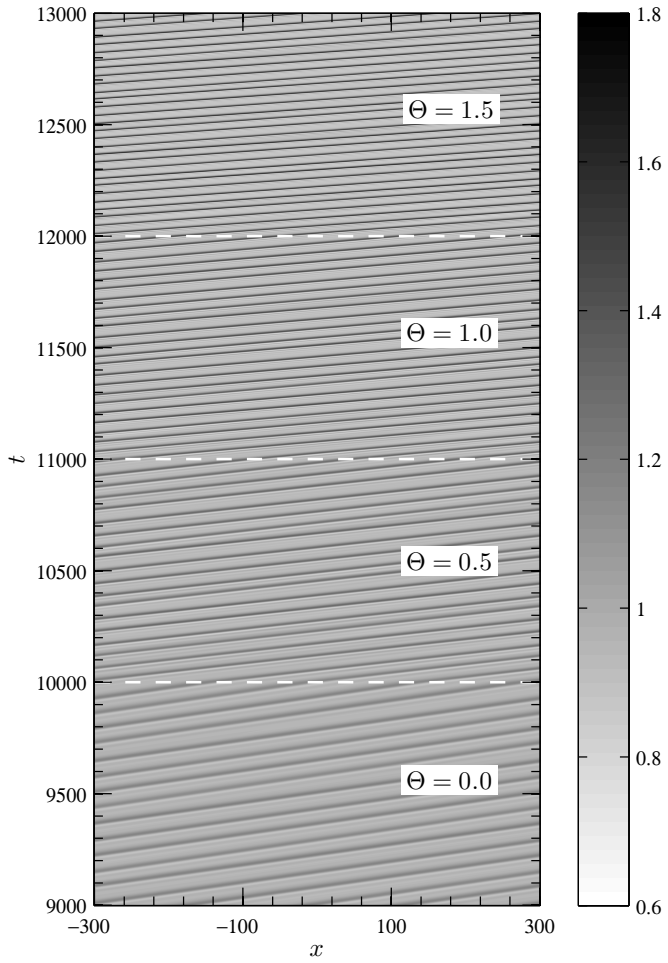


Figure 17: Space-time plot of the gas-liquid interface at $Re = 5$ for various strengths of the gas shear, with $\theta = \pi/2$, $Ka = 1988.5$ and $N = 0.4$. Brighter regions correspond to small amplitudes, and darker regions correspond to large amplitudes. Ripples can be seen clearly when the figure is zoomed in.

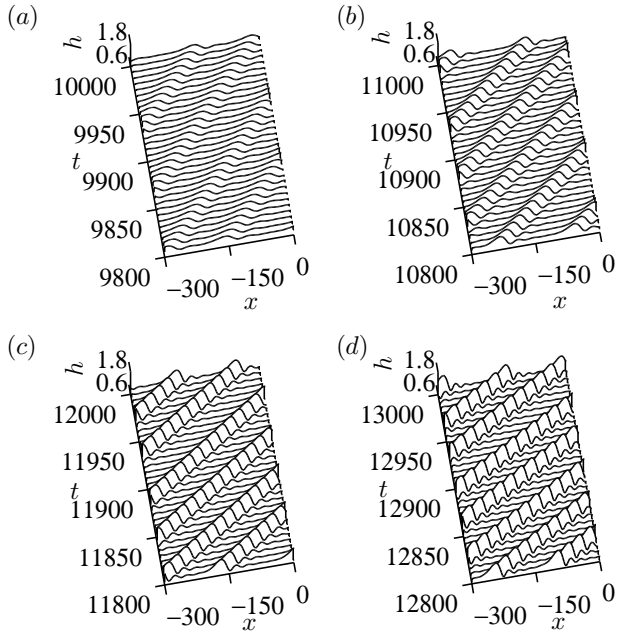


Figure 18: Time evolution of the gas-liquid interface, for $\Theta = 0, 0.5, 1.0$ and 1.5, or, equivalently, U_f^*=0, 0.94, 1.33 and 1.63 m/s, with $\theta = \pi/2$, $Ka = 1988.5$ and $N = 0.4$.

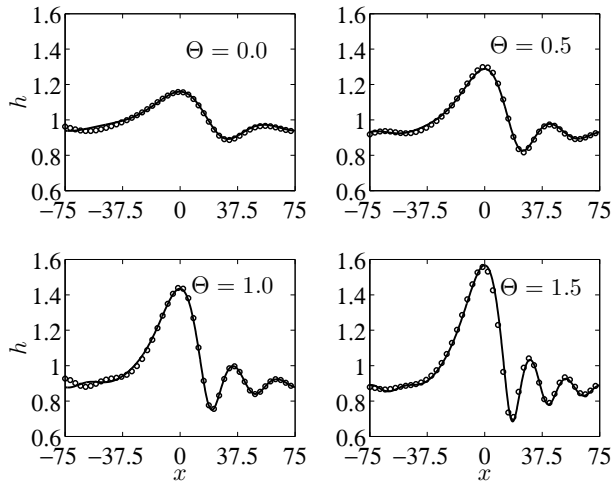


Figure 19: Comparison of the wave profiles obtained by time-dependent computations on the periodic domain of dimensionless length 600 with the profiles of steady travelling waves obtained by continuation on the domain of dimensionless length 150, for various values of the gas shear parameter Θ at $Re = 5.0$, with $\theta = \pi/2$, $Ka = 1988.5$ and $N = 0.4$. The solid curves correspond to steady travelling waves obtained from continuation, whereas the open circles correspond to time-dependent simulations. Note that for the time-dependent simulations there are four waves in the domain and just one of them is selected and shown in each of the panels.